RSC Advances

PAPER

View Article Online
View Journal | View Issue

Cite this: *RSC Adv.*, 2023, **13**, 1823

A dual-functional catalyst: wood-templated $BiVO_4$–CdS for wood dye wastewater†

Guangda Xia, [a] Sichen Xiao,[a] Junjie Su,[a] Hui Zhou,[a] Yu Liu*[a] and Xiaodong Zhu [b]

A large quantity of wastewater is released from wood processing, posing a serious pollution problem to the natural environment. Photocatalysis has become a reliable method for effluent purification. In this paper, balsa-templated $BiVO_4$–CdS (BBC) was synthesized by impregnation calcination and chemical deposition using wood residue as a template. Rhodamine B (RhB) is used as a wood colorant and is present in wood processing wastewater. The performance of BBC in photocatalytic degradation with simultaneous hydrogen production was identified using RhB as simulated wood dye wastewater and a sacrificial electron donor. Compared to the $BiVO_4$–CdS without a template, the BBC exhibited higher photocatalytic degradation performance (98.32%), which was attributed to the laminar porous structure of the wood being replicated. Because of the existence of a porous structure, BBC has better adsorption properties, which accelerated photodegradation and the production process of H_2. Furthermore, surface modification with CdS nanoparticles formed Z-scheme heterojunctions, which greatly inhibited the photogenerated electron–hole compounds. When RhB provided electrons to $BiVO_4$ and CdS, it was also removed by the oxidation of h^+ and ·OH, which were simultaneously generated by balsa-templated $BiVO_4$–CdS. BBC produced hydrogen at a higher rate (61.2 μmol g^{-1} h^{-1}), realizing dual-functional photocatalysis. Therefore, the results support further development of dual-functional catalysts by the use of wood residues.

Received 25th October 2022
Accepted 3rd January 2023

DOI: 10.1039/d2ra06735h

rsc.li/rsc-advances

1. Introduction

Recently, water contamination and wasting of resources have become two main obstacles to global development. In wood processing and production, large amounts of wood processing residues and wood processing effluent are generated, causing serious waste of resources and water pollution.[1] As a wood coloring agent Rhodamine B (RhB) is widely applied when dyeing wood and producing paper.[2,3] RhB in wood dye wastewater can seriously irritate the nasal mucosa, eyes, and skin in humans if not treated in time.[4] Compare to some conventional effluent remediation methods like physical adsorption and membrane filtration treatment, photocatalytic technology exhibits higher efficiency.[5] At the same time, photocatalysis can also be used to decompose water for hydrogen production.[6] Therefore, if effluent remediation and the production of H_2 could be accomplished synergistically, the economic benefits would be greatly enhanced.[7,8] Thus, wood dye wastewater is not only waste pollution but also an available resource.

Currently, $BiVO_4$ has become an important material in photocatalytic remediation of the environment due to its narrow bandgap and strong visible light response.[9] However, its practical application in photocatalytic treatment is limited by its poor adsorption performance and the tendency of photoexcited carriers to compound.[10,11] CdS is widely used as a hybrid element for semiconductor compounding.[12,13] However, the coupling of the two still suffers from the lack of capacity to adsorb for pollutant molecules.[14]

Plenty of reports declare that different micromorphologies affect the adsorption properties of $BiVO_4$.[15] For example, $BiVO_4$ artificial leaves that replicate the unique leaf-like morphology[16] and corn straw templates of $BiVO_4$ (ref. 17) exhibited stronger adsorption capacity than that of pure $BiVO_4$. Inheriting the microstructure of natural materials is a way to modify the micromorphology of photocatalytic materials. However, high costs and complicated processes limit the majority template catalysts out of the laboratory and applied in large-scale practical production. Therefore, in a practical production sense, it is considerable to design and search for economical and sustainable materials as templates. In the natural world, wood is abundant and has a complex and regular layered porous structure, including nanoscale molecular fibres, micron-scale transverse rays, and millimetre-scale ductal pores. These factors make wood a good photocatalytic biomimetic template.[18–20] However, plenty of wood processing residues are

[a]*College of Material Science and Engineering, Northeast Forestry University, Harbin 150040, China. E-mail: liuyu820524@126.com*

[b]*Key Laboratory of Bio-based Material Science and Technology (Northeast Forestry University), Ministry of Education, Harbin 150040, China*

† Electronic supplementary information (ESI) available. See DOI: https://doi.org/10.1039/d2ra06735h

generated in the production and processing every year, with sawmill residues ranging from 35 to 45% depending on moisture content, wood species, log size, and production equipment; fibreboard or oriented strandboard production accounts for 4–12% of wood processing residues, with edge trimming of plywood and splicing of blockboard resulting in an increase of wood processing residues (45%); and approximately 40–50% of the input wood material can be recovered as useable fibre in the pulp manufacturing process.[21,22] Hence, by using wood processing residues as a template to prepare photocatalysts for treating wood dyeing wastewater, the waste of valuable wood resources will be reduced.

In this study, a $BiVO_4$–CdS catalyst with a balsa wood was obtained by impregnation-calcination and chemical deposition. The dual-functional of balsa-templated $BiVO_4$–CdS were investigated through the removal and synergistic H_2 production of RhB. Finally, the photogenerated electron–holes migration mode and principle of photocatalysis in balsa-templated $BiVO_4$–CdS were clarified by trapping experiments and energy band analysis. This work provides a promising approach for the development of dual-functional biomass-templated photocatalysts.

2. Materials and methods

2.1 Materials

$Bi(NO_3)_3 \cdot 5H_2O$, NH_4VO_3, tetramethylammonium hydroxide aqueous solution (TMAH 25%), thiourea (CH_4N_2S), and $Cd(CH_3COO)_2 \cdot 2H_2O$ were all purchased from McLean Reagent Co. Glycerin ($C_3H_8O_3$); anhydrous ethanol (C_2H_5OH), deionized water with a conductivity of 0.055 μS cm^{-1}, and nitric acid (65%) were all purchased from Tianjin Fuyu Fine Chemical Co. RhB ($C_{28}H_{31}ClN_2O_3$) was purchased from Fuchen (Tianjin) Chemical Reagent Co. All of the reagents were analytical grade and used without further purification. All balsa wood samples were 20 mm × 20 mm × 2 mm in size, and the balsa wood with an air-dry density of 0.14 g cm^{-3} was from the training and practice base for undergraduate innovation at Northeast Forestry University.

2.2 Synthesis of the different photocatalysts

2.2.1 Preparation of balsa-templated $BiVO_4$. To remove the wood extracts, the balsa samples were treated in hot water at 60 °C for 3 h, and then the balsa samples were placed in a drying oven at 60 °C for 6 h. The pretreated balsa samples were rinsed with deionized water and immersed in $BiVO_4$ precursor solution for four days at room temperature. After the impregnation was completed, the balsa samples were repeatedly rinsed with anhydrous ethanol and deionized water. The treated balsa samples were then placed in a drying oven at 50 °C for 24 h. Finally, the treated balsa samples were calcined at 600 °C for 6 h. Balsa-templated $BiVO_4$ was thus obtained. The $BiVO_4$ precursor solution: solution A is a mixture of $Bi(NO_3)_3 \cdot 5H_2O$ (40 mmol), ethanol (80 ml), and glycerol (60 ml); solution B is a mixture of NH_4VO_3 (40 mmol) and TMAH (20 ml); add solution B to solution A drop by drop at 70 °C while adding nitric acid drop by drop until the yellow precipitate dissolved.

2.2.2 Preparation of balsa-templated $BiVO_4$–CdS. Different amounts of $Cd(CH_3COO)_2 \cdot 2H_2O$ were dissolved in 50 ml of deionized water. The balsa-templated $BiVO_4$ (0.25 mmol) was ultrasonically dispersed in the above liquid for 0.5 h. Then CH_4N_2S in the same molar ratio as $Cd(CH_3COO)_2 \cdot 2H_2O$ was added to the above suspension. After the mixture was heated at 90 °C for 2.5 h, the obtained samples were rinsed with anhydrous ethanol and deionized water, and then placed in a drying oven at 70 °C for 12 h (Fig. 1). The weight ratios between $BiVO_4$ and CdS were controlled at 2 : 1, 1 : 1, 1 : 2 and 1 : 4, and the prepared catalysts were marked as BBC-1, BBC-2, BBC-3, and BBC-4, respectively.

To set up control samples, $BiVO_4$, CdS, and $BiVO_4$–CdS (1 : 2) (without template) were prepared. The $BiVO_4$ precursor solution (as described in Section 2.2.1) was dried at 80 °C for 48 h in a drying oven. Then solid residues were calcined at 600 °C for 6 h. $BiVO_4$ was successfully obtained. $Cd(CH_3COO)_2 \cdot 2H_2O$ (1 mmol) was dissolved in 50 ml of deionized water. Then 10 ml of 0.1 mol L^{-1} CH_4N_2S was dipped into the above liquid with vigorous stirring for 20 min. After the mixture was heated at 90 °C for 2.5 h and placed in a dark location for 24 h, the obtained samples were collected by centrifugation and rinsed with anhydrous ethanol and deionized water, then dried at 70 °C for 12 h. CdS was successfully obtained. $BiVO_4$–CdS (1 : 2) (without template) was labeled as BC.

2.3 Characterization

The crystallographic phase of all samples was proofed by a multifunctional powder X-ray diffractometer (XRD, X'Pert3-Powder, Netherlands) with the following test conditions: Cu as the target radiation source ($\lambda = 0.15406$ nm), 40 kV, 40 mA, and scanning angle of 5–90°. Microstructure and morphology of all samples were recorded using field emission scanning electron microscopy (FESEM, JSM-7500F, Japan, acceleration voltage: 5 kV) and transmission electron microscopy (TEM, JEM-2100, Japan, acceleration voltage: 200 kV). Elemental composition and distribution on the sample surface were determined by Energy Dispersive Spectroscopy (EDS). The light absorption wavelengths of all samples were determined by UV-vis spectrophotometer (Agilent Cary100). The N_2 adsorption–desorption isotherms of the prepared samples were tested using a fully automated specific surface area and porosity analyzer (Micromeritics ASAP 2460, USA). Photoluminescence (PL) spectra of the sample were tested on a steady-state/transient fluorescence spectrometer (FLS1000, Edinburgh Instruments). The transient current response spectra (*I–T*) and electrochemical impedance spectra (EIS) were measured on an electrochemical workstation (CHI 760E) using a standard three-chamber electrode with a Pt electrode as a counter electrode, Ag/AgCl as a reference electrode, and ITO as a working electrode. Aqueous 0.5 M Na_2SO_4 solution was selected as the electrolyte and the frequency range was 0.1 Hz to 100 kHz.

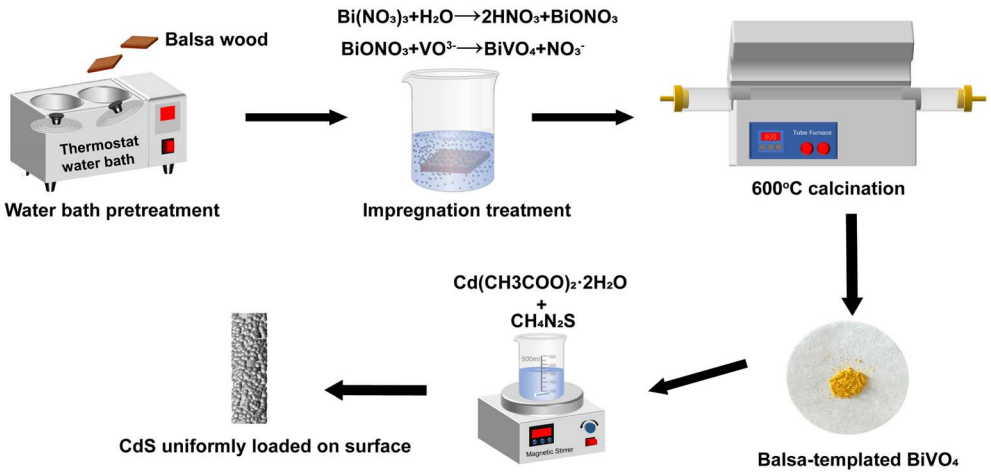

Fig. 1 Schematic diagram of wood template $BiVO_4$–CdS preparation procedure.

2.4 Photocatalytic activity measurements

All photocatalytic hydrogen production tests were carried out in a Pyrex glass reaction cell connected to a closed gas-circulation and evacuation system (Perfect Light, Beijing, Labsolar-6A). Thirty milligrams of catalyst was dispersed in fifty milliliters of aqueous RhB solution with different concentrations, and then different loadings of Pt were loaded onto the catalyst surface by photodeposition of H_2PtCl_6. Before irradiation, the suspensions were left in the dark for 1 h to reach adsorption resolution equilibrium. Five millilitres of the solution was extracted using a 0.22 μm filter membrane and the supernatant was centrifuged to calculate the removal rate of RhB using a UV-visible spectrophotometer (UV-1000, Shanghai) to compare the adsorption capacity of each catalyst. The suspensions were then ventilated several times with Ar and irradiated with a 300 W Xe-lamp (PLS-SXE300+). A cut-off filter was used to simulate visible light (λ > 420 nm) irradiation. Hydrogen production was analyzed using an online gas chromatograph (GC9790II) with a thermal conductivity detector (TCD). Finally, at the end of the reaction, the degradation rate of RhB was calculated by the spectrophotometric method. The cyclic experiments were completed by four consecutive photocatalytic reactions. The amount of scavenger used in the trapping experiments was 1 mM.

3. Results and discussion

3.1 Characterization of balsa-templated $BiVO_4$–CdS

The crystalline phases of the as-prepared photocatalysts were initially identified by XRD. The XRD pattern of pure $BiVO_4$ was identified to be compatible with the monoclinic scheelite (JCPDS No. 14-0688).[23,24] The XRD result of CdS indicated the presence of the hexagonal phase (JCPDS No. 77-2306).[25] The XRD pattern of BBC was similar to that of BC, which indicated that the balsa template does not affect the crystalline phase of the $BiVO_4$–CdS heterojunction (Fig. 2). As the loading of CdS increases, the intensity of the characteristic peak of the hexagonal phase steadily increases (2θ = 25–28°), indicating that CdS was successfully loaded on $BiVO_4$. These results clarified that the BBC catalyst was successfully prepared.

The chemical binding conditions of $BiVO_4$ and CdS can be identified by XPS. The XPS spectrum of BBC (Fig. 3a) shows that Cd, S, Bi, V, and O are the main elements of BBC. Bi^{3+} in $BiVO_4$ (Fig. 3b) is observed with two high peaks at 158.58 eV (Bi 4f 7/2) and 163.88 eV (Bi 4f 5/2).[26] Compared to both, the XPS peaks of Bi 4f in BBC are shifted to 158.28 eV and 163.48 eV. The XPS signal of O 1s in $BiVO_4$ (Fig. 3d) is found at characteristic peaks of 529.28 eV and 531.38 eV. The binding energies of O 1s in BBC are shifted to 529.18 eV and 531.58 eV, respectively, which represent lattice oxygen and surface-adsorbed oxygen.[27] After replicating the microstructure of balsa wood, the adsorption capacity of BBC on dissolved oxygen was greatly improved, which was reflected in the peak intensity of BBC increased at 531.58 eV. The positions of the characteristic peaks of Bi, V, and O demonstrate the successful synthesis of the monoclinic $BiVO_4$. The peaks of Cd^{2+} in CdS (Fig. 3e) are 404.98 eV and 411.68 eV (Cd 3d 5/2). The Cd 3d in BBC shifts to 404.78 eV and 411.48 eV, respectively.[28] The XPS pattern of Cd and S indicate that hexagonal CdS was uniformly loaded on the $BiVO_4$ surface.[29] Additionally, the positive shift of the characteristic peaks of V 2p (Fig. 3c) in BBC and the shift of the characteristic peaks of Bi 4f, S 2p, and Cd 3d to lower energies indicate the effective chemical interaction and good binding between $BiVO_4$ and CdS,[30,31] which is consistent with the XRD results.

The inheriting of wood microstructure in $BiVO_4$ was studied by SEM. By replicating the microscopic morphology of the wood (Fig. 4b and c), $BiVO_4$–CdS changed from the original irregular arrangement (Fig. 4a) to a tubular organization with a diameter of approximately 7–15 μm, growing along the longitudinal wood ray cavities of the wood. When balsa wood samples were impregnated in $BiVO_4$ precursor solution, plenty of the solution entered the wood cells and occupied the space along the wood ray channels (Fig. S1†); thus, most of the internal structure of the wood was preserved after calcination. In addition, CdS nanoparticles are uniformly bound to the surface of $BiVO_4$ by the high magnification SEM images. The EDS data (Fig. 4e)

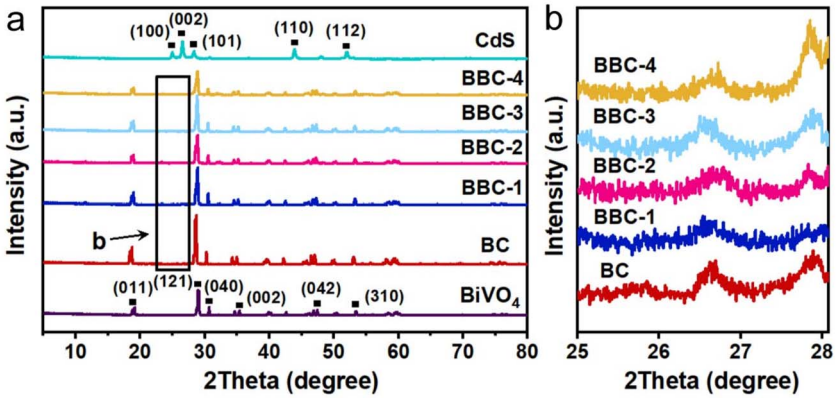

Fig. 2 (a) XRD patterns of the prepared catalysts and (b) XRD patterns of BC, BBC-1, BBC-2, BBC-3, and BBC-4 with 2θ of 25–28°.

demonstrates the presence of Bi, V, O, Cd, and S elements in BBC, while CdS is modified on $BiVO_4$, which is consistent with the XPS results. The HRTEM image of BBC (Fig. 4d) shows that the lattice spacing of 0.31 nm corresponds to the (121) crystal plane of monoclinic phase $BiVO_4$,[32] while the lattice spacing of 0.32 nm corresponds to the (101) crystal plane of the hexagonal phase CdS. The TEM results further confirm the good binding of $BiVO_4$ and CdS.[29]

The pore condition of the photocatalysts was further analyzed by N_2 adsorption–desorption experiment (Fig. 5). The calculated specific surface areas of $BiVO_4$, BC, BBC-1, BBC-2, BBC-3, and BBC-4 were 6.48, 7.11, 12.33, 20.48, 28.09, and

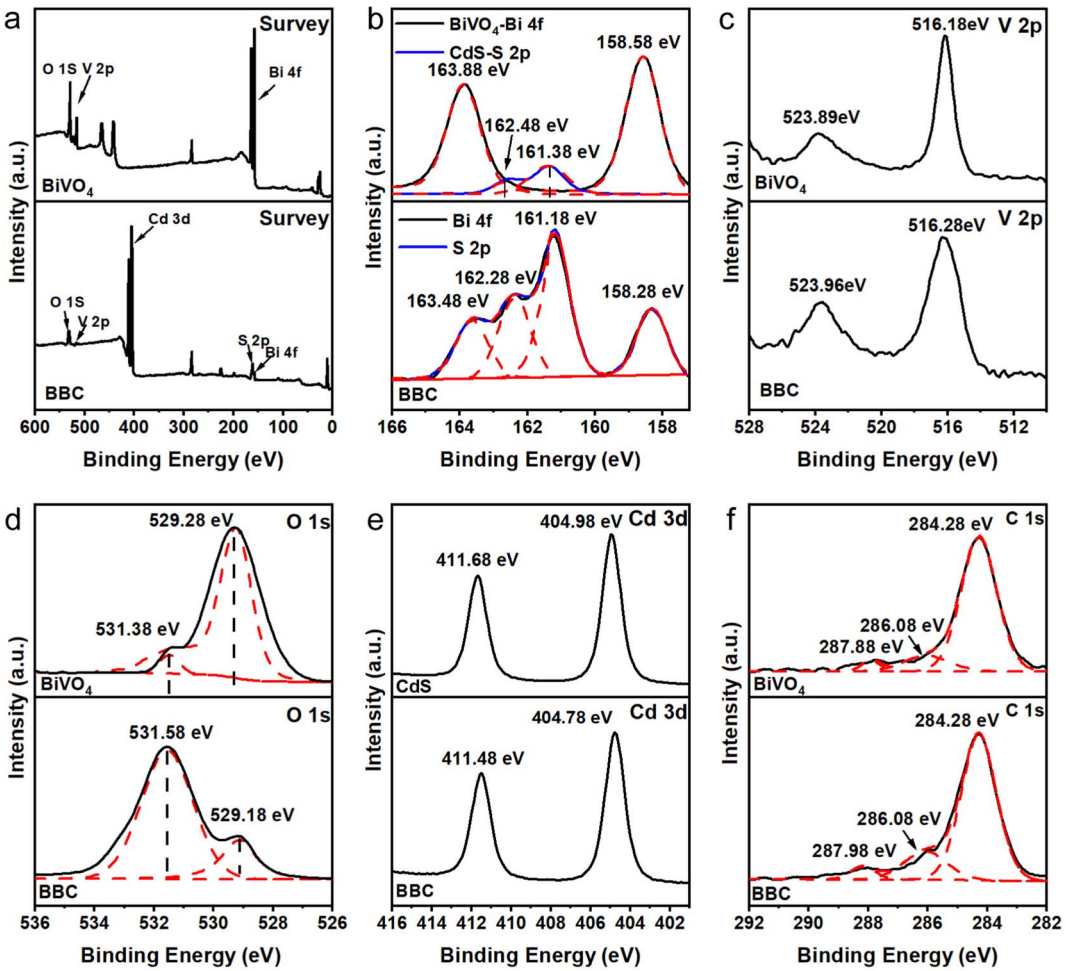

Fig. 3 Survey XPS spectra (a) and high-resolution XPS spectra of Bi 4f, S 2p (b), V 2p (c), O 1s (d), Cd 3d (e) and C 1s (f).

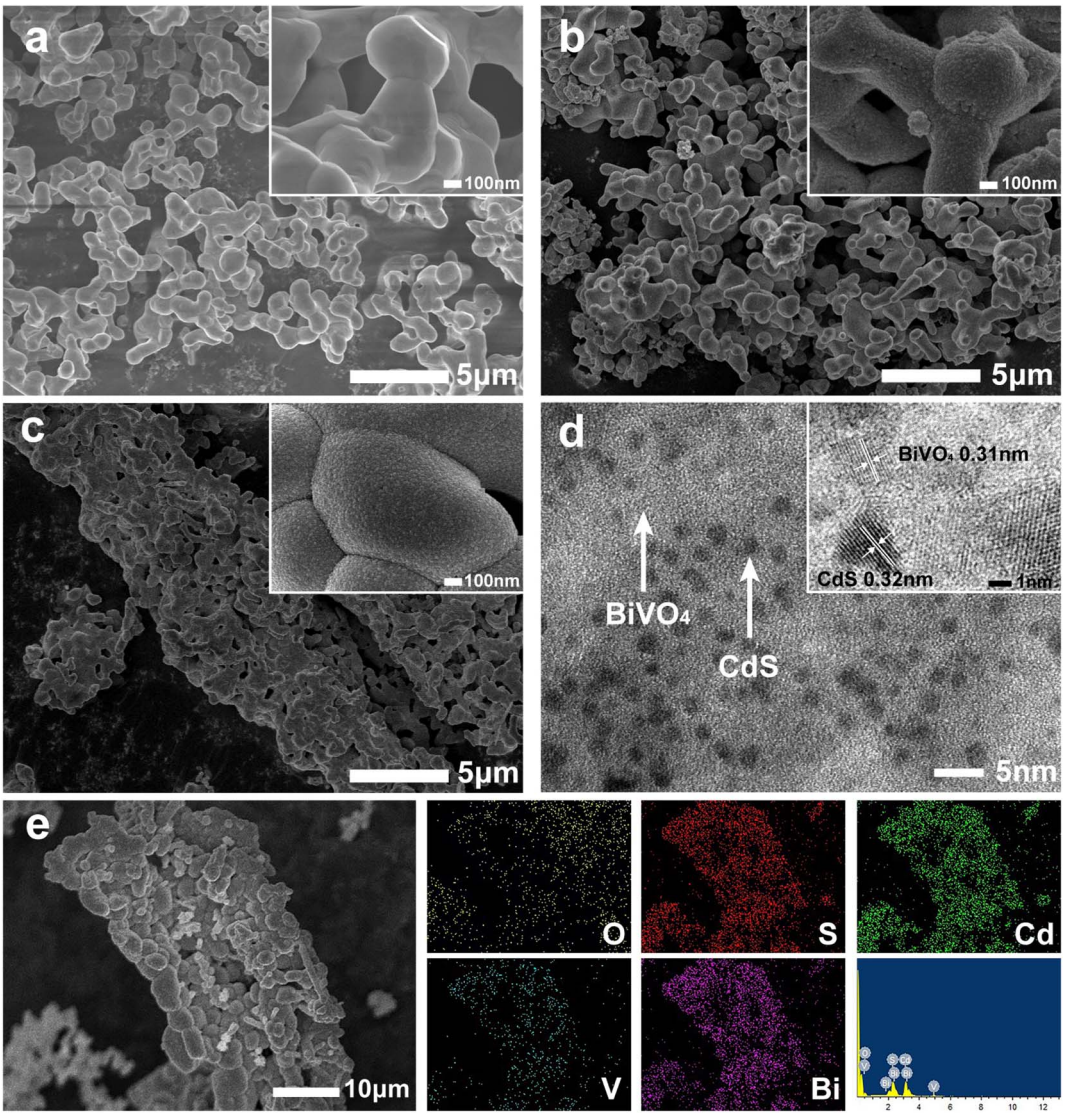

Fig. 4 SEM images of $BiVO_4$ (a), BC (b), and BBC-3 (c); TEM image and HRTEM image of BBC-3 (d); EDS pattern and elemental mapping of BBC-3 (e).

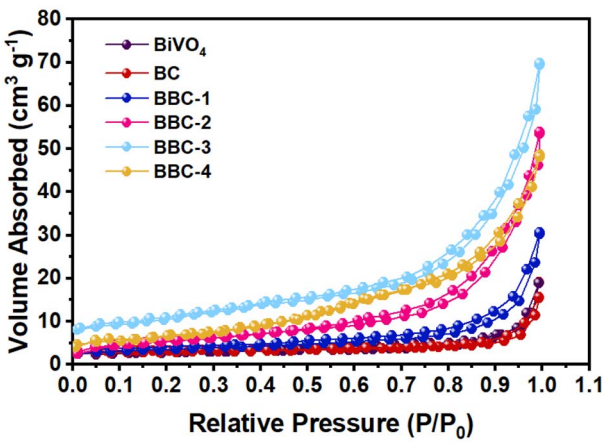

Fig. 5 N_2 adsorption–desorption isotherms of the prepared catalysts.

21.76 $m^2\ g^{-1}$, respectively. The SEM images show that the catalyst surface is covered with small nanoscale pores (10–20 nm) and other slit-type pore channels are formed due to the accumulation of agglomerates on each other. Generally, when the specific surface area of the material is large, plenty of pollutant molecules are easily absorbed by the material. The rapid contact between pollutants and photogenerated strong oxidizing substances speeds the photocatalytic progress.[33,34]

The light absorption band gap variation was analyzed by DRS. All catalysts have good absorption of the visible light (Fig. 6a). The absorption wavelengths of the composite catalysts all lie between the $BiVO_4$ (510 nm) and CdS (584 nm) (Table S1†).

At the same time, all the composite catalysts produce different degrees of redshift compared with that of $BiVO_4$, in which BBC-3 exhibited the largest absorption expansion. Because of the interfacial interaction between $BiVO_4$ and CdS,

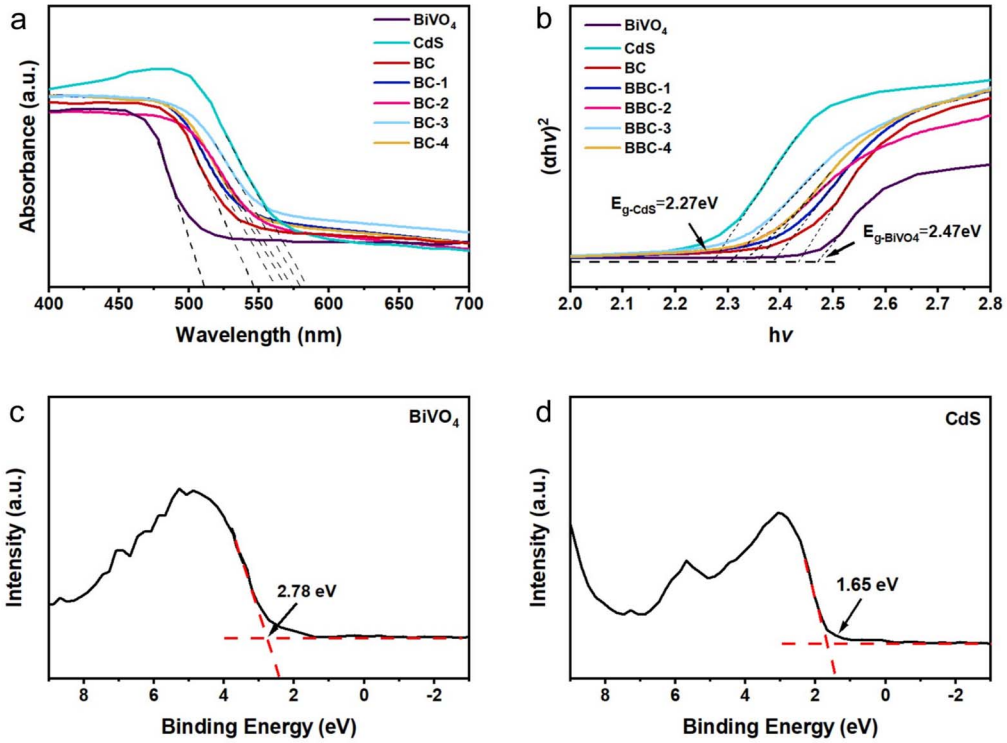

Fig. 6 (a) UV-vis DRS of the prepared catalysts and (b) the corresponding $(\alpha h\nu)^2$ *vs.* $h\nu$ plots. Valence-band XPS spectrum of $BiVO_4$ (c) and CdS (d).

the absorbing light range of the catalyst expands. At the same time, BBC exhibits the porous structure of wood, and it can transmit sufficient light and obtain a large range of light absorption, which enhances the light responsiveness. Normally, the wider the optical absorption wavelength, the stronger the photoresponse. The forbidden bandgap of the semiconductor can be estimated by eqn (1) as follows:

$$(\alpha h\nu)^{1/n} = A(h\nu - E_g) \quad (1)$$

where α, h, ν, A, and E_g are the absorption coefficient, Planck's constant, optical wave frequency, constant, and forbidden bandgap, respectively. For direct-type semiconductors, $n = 1/2$; for indirect-type semiconductors, $n = 2$.[35] The calculated forbidden bandgaps (Table S1†) are 2.47 eV and 2.27 eV for pure $BiVO_4$ and CdS, respectively (Fig. 6b). From the XPS-VB spectra (Fig. 6c and d), $BiVO_{4VB,XPS} = 2.78$ eV, $CdS_{VB,XPS} = 1.65$ eV. According to $E_{VB,NHE} = \varphi + E_{VB,XPS} - 4.44$ (φ represents the work function of the XPS instrument, $\varphi = 4.3$ eV), it is calculated that $BiVO_{4VB,NHE} = 2.62$ eV, $CdS_{VB,NHE} = 1.49$ eV.[36]

3.2 Adsorption performance of the balsa-templated $BiVO_4$–CdS

After replicating the microstructure of the wood, the adsorption performance of BBC was greatly enhanced (Fig. 7a). When the adsorption resolution equilibrium was reached, the removal rate of RhB by BBC-3 was 29.26%, which was 6.5 times higher than the removal rate of BC (4.5%). It can also be seen that the concentration of RhB decreased significantly after 1 h of adsorption by BBC-3 (Fig. 7b). The adsorption efficiency of BBC was compared with that of other reported $BiVO_4$–CdS materials with different structures (Table 1). Compared to using conventional structure, using wood as a template is more advantageous in terms of adsorption. In general, the steps of semiconductor photocatalytic reactions involve the excitation of photocatalytic materials by photons with energy higher than their forbidden bandgap to produce photoexcited carriers. Then the pollution molecule adsorbed on the material surface was oxidated and reduced by these carriers.[37] If the catalyst exhibits a good adsorption capacity, then the subsequent photocatalytic reaction process will speed up (Fig. 8).

3.3 Photocatalytic performance of the balsa-templated $BiVO_4$–CdS

To verify the photocatalytic performance of the BBC, tests on photocatalytic H_2 production and simultaneous degradation of RhB were carried out. The rate of H_2 production and RhB removal increased rapidly with increasing CdS content (Fig. 8a), and the rate of H_2 production and RhB degradation reached a maximum (61.2 μmol g^{-1} h^{-1}) when $BiVO_4$: CdS was 1 : 2. The rate of H_2 production significantly decreased when the loading amount of CdS continued to increase. This occurred because the CdS loading on $BiVO_4$ forms a heterogeneous structure, which greatly inhibits the compounding of photoexcited carriers and improves the electron–hole separation efficiency. However, when the loading amount of CdS reaches a certain level, a portion of the active site is covered, which affects the

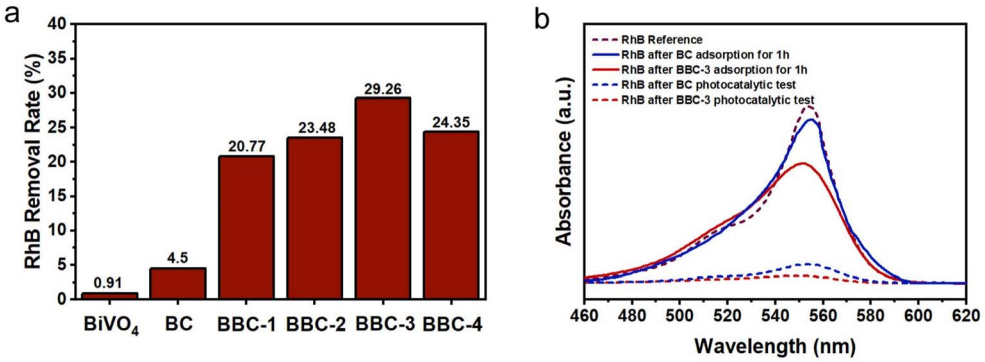

Fig. 7 RhB adsorption (a) and UV-vis spectra (b) of prepared catalysts.

photoresponse ability of the BBC under visible light. Therefore, when the $BiVO_4$: CdS ratio is 1 : 2, a better amount of CdS is loaded in the composite.

Then, the effects of different loading amounts of Pt on the H_2 production and RhB degradation efficiency were investigated using BBC-3. As shown in Fig. 8b, the rate of H_2 production and RhB degradation increased as the Pt loading increased from 0.5% to 1%, while the rate of H_2 production and RhB removal decreased a little as the Pt loading increased from 1% to 2%. This situation occurs because Pt clusters form on the surface of BBC-3 when the loading amount of Pt exceeds 1%, which reduces the availability of this part of Pt; as a result, the efficiency of photogenerated electron–hole separation decreases and the photocatalytic ability of the catalyst weakens.[41,42]

In addition, the effect of the initial concentration of RhB solution on the photocatalytic H_2 generation of BBC-3 was further studied. As the initial concentration of RhB solution increased, the rate of H_2 generation increased first and then decreased. The fastest rate of H_2 production was achieved at an initial RhB concentration of 10 mg L^{-1} (Fig. S2a†). When the dye concentration initially increases, more RhB molecules adsorb to the catalyst surface, which in turn can interact with the photogenerated electron holes more rapidly. As the RhB concentration further increases, the irradiation of some visible light through the water bodies to BBC-3 is hindered, leading to a lower rate of H_2 production.[43] Finally, the long-term stability of BBC-3 was examined by four rounds of cycling experiments (Fig. 8d). After four consecutive cycles (Fig. S2b†), the rate of H_2 generation decreased slightly (61.2 → 57.31 μmol g^{-1} h^{-1}), and the rate of synergistic degradation of RhB remained almost unchanged (98.33 → 95.27%). The results indicate that BBC-3 exhibits excellent long-term stability and photocatalytic activity.

The photogenerated electron–hole complexation rate is a key factor that affects the photocatalytic performance of photocatalysts. The photogenerated electron–hole separation of the prepared catalysts was investigated by fluorescence spectra, photocurrent response, and EIS spectra. Fig. 9a shows the PL spectra of $BiVO_4$, CdS, BC, and BBC-3. Compared with $BiVO_4$ and CdS, both BC and BBC-3 exhibit a significantly weaker fluorescence intensity, and the fluorescence intensity of BBC-3 is the weakest, indicating that photogenerated electron–hole complexation is inhibited in the presence of heterojunctions, and the electron–hole on BBC-3 exhibits the best separation efficiency.[44] Photoelectrochemical experiments were then performed, the photocurrent response of BBC-3 is much higher than those of $BiVO_4$, CdS, and BC (Fig. 9b), which indicates that photogenerated electron–holes are more readily transferred to the surface for redox reactions through the channels formed by the wood template, which is consistent with the photoluminescence results.[45] EIS spectra were used to elucidate the migration of photoexcited electron–holes. In the Nyquist plot, the arc radius represents the equivalent resistance, and the larger the arc radius, the higher the recombination of the photoexcited electron–hole.[46] The semicircular radius of BBC-3

Table 1 Adsorption performance of different structures of $BiVO_4$–CdS

Photocatalyst	Solution	Removal efficiency (adsorption equilibrium)	Reference
Balsa templated-$BiVO_4$–CdS	10 mg per L RhB	29.26%	This work
Hollow CdS/$BiVO_4$	15 mg per L RhB	0.536%	38
$BiVO_4$–CdS	20 mg per L TCH	1.435%	14
SDBC–$BiVO_4$–CdS	20 mg per L TCH	3.138%	14
PVP–$BiVO_4$–CdS	20 mg per L TCH	6.384%	14
EDTA–$BiVO_4$–CdS	20 mg per L TCH	9.221%	14
$BiVO_4$–Au@CdS	5 mg per L RhB	9.248%	39
Hierarchical construction Bi/$BiVO_4$–CdS	20 mg per L TCH	20.865%	40

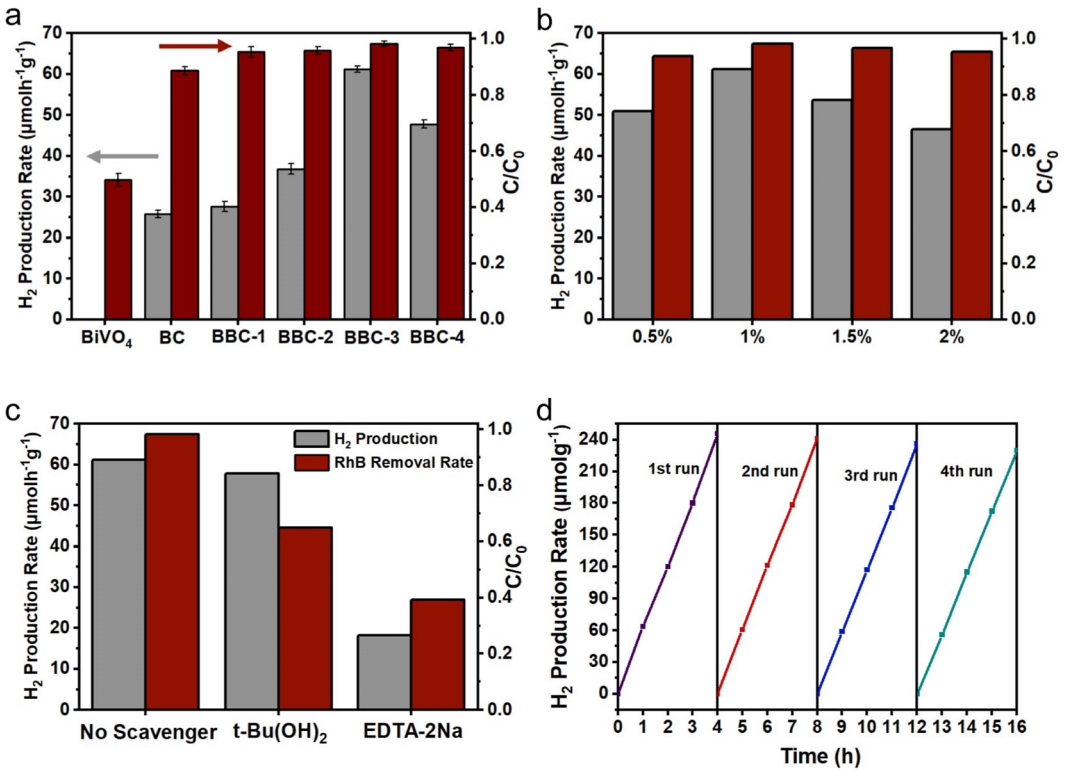

Fig. 8 Photocatalytic degradation with simultaneous hydrogen production of the prepared catalysts at 1% Pt (a) loading and different Pt loadings (b); (c) ·OH radical and h^+ trapping experiments; (d) cycling runs of photocatalytic hydrogen H_2 production over BBC-3 in RhB solution.

is smaller than those of $BiVO_4$, CdS, and BC (Fig. 9c), thus indicating that BBC-3 shows a higher migration efficiency for photogenerated carriers.

To clarify the principle of synergistic H_2 production from RhB photodegradation, trapping experiments were performed to investigate the main active species in the photocatalytic process on BBC-3. Hydroxyl radical (·OH) and hole (h^+) trapping experiments were performed by adding *t*-$Bu(OH)_2$ and EDTA-2Na, respectively. When adding *t*-$Bu(OH)_2$ to the system, the degradation rate of RhB was somewhat affected, and it was hardly affected by the efficiency of H_2 production. When EDTA-2Na was present in the system, the rate of H_2 production and the removal rate of RhB decreased greatly. The results of the active species trapping indicated that both h^+ and ·OH were involved in the RhB degradation process, while ·OH was basically not involved in the photocatalytic H_2 production process, and h^+ is the main active substances for photocatalytic degradation and photocatalytic H_2 production. These results further demonstrate that RhB acts as a sacrificial electron donor and scavenges photogenerated holes to promote H_2 production while leading to its own decomposition (Fig. S2c†).

The results of photodegradation of RhB with simultaneous production of H_2 illustrated that the complexation of CdS improved the photoresponsiveness of $BiVO_4$ and that the replication of wood micromorphology exhibited a better adsorption ability. To elucidate the photocatalytic mechanism of this system, the empirical equation $E_g = E_{VB} - E_{CB}$ was used to calculate the conduction band (CB) potentials of pure $BiVO_4$

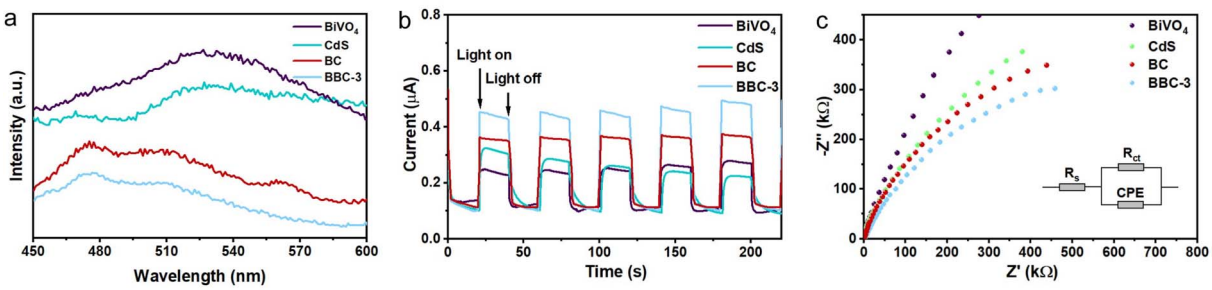

Fig. 9 PL spectra (a), photocurrent response (b), and EIS spectra (c) of $BiVO_4$, CdS, BC, and BBC-3.

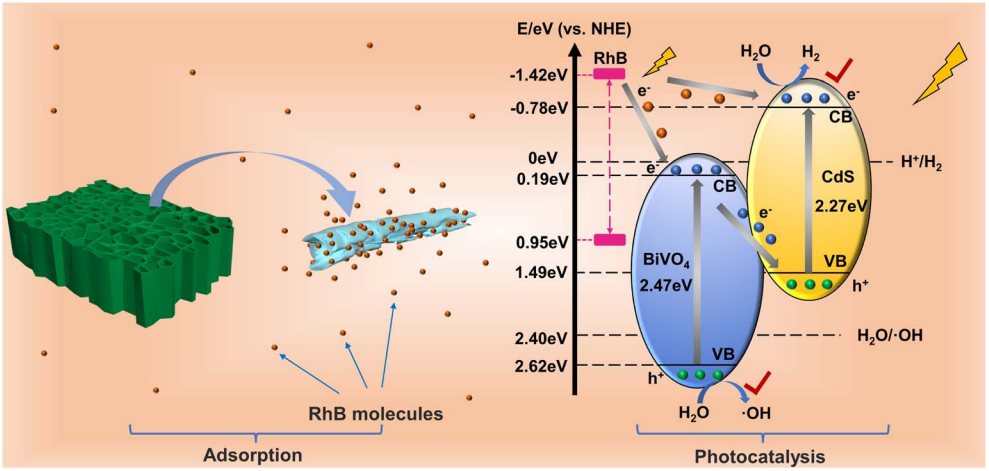

Fig. 10 Mechanism of synergistic hydrogen production by photocatalytic degradation.

and CdS.[47] According to the calculated E_{VB} of $BiVO_4$ and CdS, it is calculated that $E_{CB\text{-}BiVO4} = 0.15$ eV and $E_{CB\text{-}CdS} = -0.78$ eV (*vs.* NHE). Apparently, when $BiVO_4$ and CdS are hybridized, suitable band structures can be established to improve the electron–hole pair efficiency.

In addition, the RhB molecules adsorbed on the catalyst surface can generate electrons by photoexcitation, and the LUMO and HOMO of RhB are −1.42 and 0.95 eV, respectively.[48,49] Since the LUMO site of RhB is more negative than the CB of $BiVO_4$ and CdS, photogenerated electrons can be delivered to $BiVO_4$ and CdS. In this way, the large amount of foreign electrons that are injected increases the carrier migration rate between the catalyst interfaces, which in turn enhances the photocatalytic efficiency. The carrier transfer mode is discussed below.

If the electron transfer between $BiVO_4$ and CdS follows the traditional type II heterojunction, then the photogenerated electrons will transfer from the CB of CdS to the CB of $BiVO_4$, and the photogenerated holes will transfer from the VB of $BiVO_4$ to CdS. At this time, the electrons and holes will accumulate at the CB of $BiVO_4$ and the VB of CdS, respectively. Since the reduction potential of H_2 is more negative than the CB of $BiVO_4$, and the oxidation potential of ·OH is more positive than the VB of CdS, then H_2 and ·OH cannot be produced, which is inconsistent with the experimental results. Therefore, the transfer of carriers should follow a more reasonable mechanism, the Z-scheme transfer mechanism.

The irregular $BiVO_4$–CdS agglomerates improve the transfer efficiency of photocatalytic products and RhB molecules at the interface due to the three-dimensional pore structure of wood.[50,51] The BBC rapidly adsorbs a large number of RhB molecules, and subsequently, the RhB molecules are excited by light and generate electrons that are inputted onto the CB of $BiVO_4$ and CdS. In the heterojunction of $BiVO_4$–CdS, the electrons in the CB of $BiVO_4$ can be rapidly moved to the VB of CdS to regroup with the photogenerated holes it produces. At this point, the photogenerated holes of $BiVO_4$ and the photogenerated electrons of CdS are retained. The holes in the VB of $BiVO_4$ and the electrons in the CB of CdS produce ·OH and H_2 during photoexcitation, which is consistent with the photocatalytic results (Fig. 10). RhB was removed by its own supply of electrons while being oxidized by ·OH. Through this photogenerated carrier transfer mode, the composite $BiVO_4$–CdS exhibits better redox performance to degrade pollutants while generating hydrogen, making BBC-3 a good dual-functional catalyst.

4. Conclusions

Balsa-templated $BiVO_4$–CdS was successfully synthesized by impregnation calcination and chemical deposition methods. The two processes, photocatalytic dye degradation and hydrogen production, were integrated into a single system. Compared with the untemplated $BiVO_4$–CdS (4.5%), the balsa-templated $BiVO_4$–CdS exhibited an extremely high adsorption capacity (29.26%). Additionally, $BiVO_4$ and CdS formed Z-scheme heterojunctions, thus exhibiting superior photocatalytic hydrogen production and degradation performance. The balsa-templated $BiVO_4$–CdS produced H_2 at a higher rate (61.2 μmol g^{-1} h^{-1}), while the RhB removal rate (98.32%) was higher under visible light. To the best of our knowledge, few reports have investigated biomass template dual-functional catalytic systems. At the same time, resources are sustainably recycled by using wood residues as the template. In addition, synergistic hydrogen production for the degradation of other dyes will be further investigated in future work. This study contributes to the goal of developing novel dual-functional catalysts that offer a new possibility for water remediation and energy development.

Author contributions

Guangda Xia: investigation, resources, validation, data curation, formal analysis, writing – original draft, visualization. Sichen Xiao: investigation, resources, validation, data curation. Junjie Su: investigation, supervision, software, formal analysis,

visualization. Hui Zhou: methodology, supervision. Yu Liu: conceptualization, methodology, validation, formal analysis, writing – review & editing, visualization, supervision, project administration, funding acquisition. Xiaodong Zhu: conceptualization, methodology, writing – review & editing, supervision.

Conflicts of interest

The authors declare that they have no known competing financial interests or personal relationships that could have appeared to influence the work reported in this paper.

Acknowledgements

This work is financially supported by National Natural Science Foundation of China (Grant 32201481), Fundamental Research Funds for the Central Universities (2572022BB07), Innovative Entrepreneurial Projects for College Students (202210225092).

References

1 A. Vlyssides, E. M. Barampouti, S. Mai and A. Vlyssides, *Environ. Eng. Sci.*, 2008, **25**, 327–332.
2 T. H. Yen Doan, T. P. Minh Chu, T. D. Dinh, T. H. Nguyen, T. C. Tu Vo, N. M. Nguyen, B. H. Nguyen, T. A. Nguyen and T. D. Pham, *J. Anal. Methods Chem.*, 2020, **2020**, 6676320.
3 E. García-López, A. Alcázar, A. M. Moreno and C. Cid, Color-Producing Extremophiles, *Bio-Pigm. Biotechnol. Implementations*, 2017, **3**, 61–86.
4 M. S. Field, R. G. Wilhelm, J. F. Quinlan and T. J. Aley, *Environ. Monit. Assess.*, 1995, **38**, 75–96.
5 G. Chandrabose, A. Dey, S. S. Gaur, S. Pitchaimuthu, H. Jagadeesan, N. Braithwaite, V. Selvaraj, V. Kumar and S. Krishnamurthy, *Chemosphere*, 2021, **279**, 130467.
6 J. W. Hong, *Catalysts*, 2021, **11**, 848.
7 Z. D. Wei, M. Q. Xu, J. Y. Liu, W. Q. Guo, Z. Jiang and W. F. Shangguan, *Chin. J. Catal.*, 2020, **41**, 103–113.
8 H. Wang, Y. Wu, M. Feng, W. Tu, T. Xiao, T. Xiong, H. Ang, X. Yuan and J. W. Chew, *Water Res.*, 2018, **144**, 215–225.
9 I. Grigioni, G. Di Liberto, M. V. Dozzi, S. Tosoni, G. Pacchioni and E. Selli, *ACS Appl. Energy Mater.*, 2021, **4**, 8421–8431.
10 Y. Zhang, J. Q. Yu, A. Kudo and X. S. Zhao, *Chin. J. Catal.*, 2008, **29**, 624–628.
11 M. N. Guo, Y. Wang, Q. L. He, W. J. Wang, W. M. Wang, Z. Y. Fu and H. Wang, *RSC Adv.*, 2015, **5**, 58633–58639.
12 L. Zou, X. Wang, X. Xu and H. Wang, *Ceram. Int.*, 2016, **42**, 372–378.
13 M. Zhukovskyi, P. Tongying, H. Yashan, Y. Wang and M. Kuno, *ACS Catal.*, 2015, **5**, 6615–6623.
14 Z. Wu, Y. Xue, X. He, Y. Li, X. Yang, Z. Wu and G. Cravotto, *J. Hazard. Mater.*, 2020, **387**, 122019.
15 Y. Lu, H. Shang, F. Shi, C. Chao, X. Zhang and B. Zhang, *J. Phys. Chem. Solids*, 2015, **85**, 44–50.
16 R. Yang, R. Zhu, Y. Fan, L. Hu and Q. Chen, *RSC Adv.*, 2019, **9**, 14004–14010.
17 M. Wang, H. Zheng, J. Liu, D. Dong, Y. Che and C. Yang, *Mater. Sci. Semicond. Process.*, 2015, **30**, 307–313.
18 Z. Liu, T. Fan, J. Gu, D. Zhang, X. Gong, Q. Gu and J. Xu, *Mater. Trans.*, 2007, **48**, 878–881.
19 Z. Liu, T. Fan, W. Zhang and D. Zhang, *Microporous Mesoporous Mater.*, 2005, **85**, 82–88.
20 T. Yang, Y. Liu, G. Xia, X. Zhu and Y. Zhao, *J. Cleaner Prod.*, 2021, **329**, 129726.
21 U. Saal, H. Weimar and U. Mantau, in *Biorefineries*, ed. K. Wagemann and N. Tippkotter, 2019, vol. 166, pp. 27–41.
22 G. Faraca, A. Boldrin and T. Astrup, *Waste Manag.*, 2019, **87**, 135–147.
23 L. Zhang, D. Chen and X. Jiao, *J. Phys. Chem. B*, 2006, **110**, 2668–2673.
24 H. Fan, D. Wang, Z. Liu, T. Xie and Y. Lin, *Dalton Trans.*, 2015, **44**, 11725–11731.
25 D. Wang, L. Guo, F. Fu, Y. Liang and H. Shen, *New J. Chem.*, 2016, **40**, 8614–8624.
26 F. Fang, Y. Zhang, J. Bai, J. Li, X. Mei, C. Zhou, M. Zhou and B. Zhou, *Environ. Pollut.*, 2020, **267**, 115605.
27 P. G. Ingole, H. Y. Sang, P. G. Ingole, W. K. Choi and H. K. Lee, *J. Mater. Chem. A*, 2015, **3**, 7888–7899.
28 Z. Yu, Y. Xie, G. Liu, G. Lu, X. Ma and H. Cheng, *J. Mater. Chem. A*, 2013, **1**, 2773–2776.
29 L. J. Zhang, S. Li, B. K. Liu, D. J. Wang and T. F. Xie, *ACS Catal.*, 2014, **4**, 3724–3729.
30 Y. Zhang, Y. Guo, H. Duan, L. Hua and H. Liu, *Phys. Chem. Chem. Phys.*, 2014, **16**, 24519–24526.
31 S. Bao, Q. Wu, S. Chang, B. Tian and J. Zhang, *Catal. Sci. Technol.*, 2016, **7**, 124–132.
32 X. Li, J. Sun, Q. Zhao, M. O. Tade and S. Liu, *J. Mater. Chem. A*, 2015, **3**, 21655–21663.
33 W. Zhou, Z. Yin, Y. Du, X. Huang, Z. Zeng, Z. Fan, H. Liu, J. Wang and H. Zhang, *Small*, 2013, **9**, 140–147.
34 G. Yang, D. Chen, H. Ding, J. Feng, J. Zhang, Y. Zhu, S. Hamid and D. W. Bahnemann, *Appl. Catal., B*, 2017, **219**, 611–618.
35 G. Zhang, D. Chen, N. Li, Q. Xu, H. Li and J. He, *Appl. Catal., B*, 2018, **232**, 164–174.
36 Y. Xu and M. Schoonen, *Am. Mineral.*, 2000, **85**, 543–556.
37 A. L. Linsebigler, G. Lu and J. T. Yates, *Chem. Rev.*, 1995, **95**, 735–758.
38 Y. Lin, D. Pan and H. Luo, *Mater. Sci. Semicond. Process.*, 2021, **121**, 105453.
39 F. Ye, H. Li, H. Yu, S. Chen and X. Quan, *Appl. Catal., B*, 2018, **227**, 258–265.
40 Y. Xue, Z. Chen, Z. Wu, F. Tian and B. Yu, *Sep. Purif. Technol.*, 2021, **275**, 119152.
41 Z. Lu, W. Song, O. Chao, H. Wang, D. Zeng and C. Xie, *RSC Adv.*, 2017, **7**, 33552–33557.
42 F. Fina, H. Ménard and J. T. S. Irvine, *Phys. Chem. Chem. Phys.*, 2015, **17**, 13929–13936.
43 S. Kampouri, T. N. Nguyen, M. Spodaryk, R. G. Palgrave, A. Züttel, B. Smit and K. C. Stylianou, *Adv. Funct. Mater.*, 2018, **28**, 1806368.
44 X. Wu, J. Zhao, L. Wang, M. Han, M. Zhang, H. Wang, H. Huang, Y. Liu and Z. Kang, *Appl. Catal., B*, 2017, **206**, 501–509.

45 W. Zhao, Z. Wei, G. Zhu, T. Lin and Q. H. Fu, *Dalton Trans.*, 2016, **45**, 3888–3894.
46 X. Ding, Y. Wang, H. Shi, L. Huang, Y. Zuo and S. Kang, *Appl. Surf. Sci.*, 2017, **391**, 202–210.
47 X. Chen, Y. Zhou, Q. Liu, Z. Li and J. Liu, *ACS Appl. Mater. Interfaces*, 2012, **4**, 3372–3377.
48 Z. Chen, J. Zhao, J. Chen, Y. Zhang, D. Chen, Q. Wang and D. Xia, *Sep. Purif. Technol.*, 2021, **258**, 118007.
49 R. Bibi, Q. Shen, L. Wei, D. Hao, N. Li and J. Zhou, *RSC Adv.*, 2018, **8**, 2048–2058.
50 D. R. Rolison, *Science*, 2003, **299**, 1698–1702.
51 S. Dapurkar, S. Badamali and P. Selvam, *Catal. Today*, 2001, **68**, 63–68.